

Li-diffusion accelerates grain growth in intercalation electrodes: a phase-field study

Ananya Renuka Balakrishna*, Yet-Ming Chiang and W. Craig Carter

Department of Materials Science and Engineering, Massachusetts Institute of Technology, Cambridge, MA02139, USA

*Email: ananyarb@mit.edu

Abstract

Grain boundary migration is driven by the boundary's curvature and external loads such as temperature and stress. In intercalation electrodes an additional driving force results from Li-diffusion. That is, Li-intercalation induces volume expansion of the host-electrode, which is stored as elastic energy in the system. This stored energy is hypothesized as an additional driving force for grain boundaries and edge dislocations. Here, we apply the 2D Cahn-Hilliard – phase-field-crystal (CH-PFC) model to investigate the coupled interactions between highly mobile Li-ions and host-electrode lattice structure, during an electrochemical cycle. We use a polycrystalline FePO_4 / LiFePO_4 electrode particle as a model system. We compute grain growth in the FePO_4 electrode in two parallel studies: In the first study, we electrochemically cycle the electrode and calculate Li-diffusion assisted grain growth. In the second study, we do not cycle the electrode and calculate the curvature-driven grain growth. External loads, such as temperature and stress, did not differ across studies. We find the mean grain-size increases by $\sim 11\%$ in the electrochemically cycled electrode particle. By contrast, in the absence of electrochemical cycling, we find the mean grain-size increases by $\sim 2\%$ in the electrode particle. These CH-PFC computations suggest that Li-intercalation accelerates grain-boundary migration in the host-electrode particle. The CH-PFC simulations provide atomistic insights on diffusion-induced grain-boundary migration, edge dislocation movement and triple-junction drag-effect in the host-electrode microstructure.

Key words: grain growth, phase-field crystal model, intercalation electrodes, batteries

Introduction

An ion storage electrode used in rechargeable batteries typically consists of polycrystalline (secondary) particles. The electrode's volume can substantially expand (e.g., up to $\sim 10\%$) as the working ion concentration is varied [1]. This expansion is often anisotropic [2], and sometimes leads to mechanical fracture of the electrode [3]. Mechanical fracture impacts a battery's electrochemical properties, such as accessible capacity, rate capability, and lifetime [4]. An electrode's physical properties, such as fracture toughness and electrochemical potential, correlate with its grain size in polycrystalline particles [5], [6]. Thermal loads, as well as dopants, are known to affect grain size [7,8]. At elevated temperatures, in-situ electric currents also cause grain growth in electrochemical systems [7] [9]. To date, we are not aware of any work that explores how cyclic intercalation affects grain growth in a battery electrode at ambient temperatures. Here we examine whether – and, if so, to what extent – electrochemical cycling enhances grain growth, using FePO_4 / LiFePO_4 as a model system.

During an electrochemical cycle, Li-ions intercalate into a host electrode, such as FePO_4 / LiFePO_4 [10]. This insertion and extraction of Li-ions (diffusing species) produces lattice strains in the host material, and transforms lattice structure at critical values of Li-compositions. In a polycrystalline electrode, these lattice transformations generate an inhomogeneous strain field [2]. In phase separating materials, such as the FePO_4 , an additional strain arises between the lithiated and delithiated phases. Handwerker et al. [11,12] propose that these internal strain fields drive grain boundaries in the host electrode. In the present work, we

apply a Cahn-Hilliard – phase-field-crystal model to demonstrate this diffusion-induced grain-boundary migration in an FePO_4 host-electrode.

Researchers have developed several theoretical models to investigate electrode microstructures in lithium batteries [13–25]. Based on length scales, these theoretical models can be broadly clustered into continuum and atomistic methods. The continuum methods, such as the phase field models, describe the time evolution of electrode microstructures. The phase field models have been applied to investigate the role of electrode-particle size on miscibility gap [15], phase separation [16] and stress generation [26]. A crystallographic phase-field model builds on the classic phase-field approach by introducing grain orientation as an additional order parameter [27]. The continuum models are developed to consider electrochemistry [19], surface morphologies [23], and coherency strains [14,17]. These methods, however, do not model individual lattice distortions. The microstructural defects such as grain boundaries are empirical parameters in these continuum methods.

Atomistic models such as the first principle methods [21] and molecular dynamics models [24, 25], provide insights on electrochemical stability of ionic compounds [21], lattice distortions [20, 22] and ionic diffusion in electrodes [24]. However, these approaches are limited in length and time scales. For example, the molecular dynamics method can typically model few hundreds of atoms. Consequently, microstructural features such as grain boundaries are computationally expensive to simulate using these atomistic approaches. Furthermore, the time scales involved in molecular dynamics computations are over thermal-vibrations. These time scales limits us to model continuum Li-diffusion. Accel-

erated molecular dynamics methods use the transition state theory to overcome the time scale limitation [28], and have been applied to simulate crystal growth [29].

Alternatively in our recent work [30], we combined a Cahn-Hilliard model with a phase-field-crystal model (CH-PFC). This model describes phase transitions and interstitial diffusion in a 2D theoretical framework. In this multiscale approach, the PFC equation models the coarse-grained lattice structure of the host-electrode material (atomistic scale). The CH equation models Li-intercalation in the electrode (continuum scale). The coupled CH-PFC model captures the host-electrode lattice transformations induced from Li-diffusion. This modeling approach enables us to investigate the time evolution of lattice arrangements in electrode particles. For example, the model simulates dislocation movement and grain-boundary migration in electrodes during an electrochemical cycle.

In this paper, we apply the 2D CH-PFC methods to model Li-intercalation in an FePO₄ electrode particle. First, we calibrate the CH-PFC model to describe the lattice geometries of FePO₄ and LiFePO₄. Using the model, we simulate a polycrystalline FePO₄ electrode particle. We next compute two parallel simulations: In the first, we electrochemically cycle the electrode particle where Li-ions intercalate into FePO₄ lattices. In the second study, we do not cycle the FePO₄ electrode particle. We compare the grain boundary migration in the two studies. We hypothesize that Li-intercalation accelerates grain-boundary migration in the cycled electrode. Throughout, we compare the CH-PFC results with the existing literature on microstructures in electrode materials.

Cahn-Hilliard – phase-field-crystal model

In this section, we briefly explain the CH-PFC model applied to FePO₄ electrodes. The details of the model are given in the appendix and in Ref. [30]. For our purposes, we note that the CH-PFC model has two order parameters: First, the peak-density field $\psi(\vec{x})$ that represents coarse-grained lattices of the host electrode [31]. The lattice points of the host electrode are constrained in space and do not hop or migrate. These lattices, however, undergo displacive transformations to represent lattice strains. Second, the composition field $c(\vec{x})$ that represents Li-intercalation (mobile species) through the host electrode.

During electrochemical cycling, the FePO₄ electrode typically phase-separates into lithium-rich (LiFePO₄) and lithium-deficient (FePO₄) phases [10]. This FePO₄ / LiFePO₄ phase transition is first order (with an abrupt change of bulk lattice constants). In experiments, however, an interphase region Li_XFePO₄ with $0 < X < 1$ has been observed to form [32, 33]. This interphase region reduces the lattice misfit at the FePO₄ / LiFePO₄ contact [32]. In the current work, we approximate the interphase region to correspond to a diffuse phase boundary. We model the lattices in the interphase region to have averaged lattice parameters intermediate to FePO₄ and LiFePO₄ lattices. Both the interstitial Li-composition $c(\vec{x})$ and the host-electrode lattice structure $\psi(\vec{x})$ continuously change across the diffuse interface. The CH-PFC model describes the normalized total free energy \mathcal{F} of a two-phase

system as:

$$\mathcal{F} = \int \{g(c) + |\nabla c|^2 + \gamma[f(r, \psi) + \frac{\psi}{2}G(\nabla_c^2)\psi]\}d\vec{x}. \quad (1)$$

In Eq. 1, $c(\vec{x})$ is the fraction of interstitial sites in FePO₄ electrode occupied by Li per unit volume. The polynomial $g(c)$ represents a regular solution model [13, 34] that describes a double well potential. The coefficients in $g(c)$ are normalized such that the double wells are at equal heights with minima at $c(\vec{x}) = 0$ and $c(\vec{x}) = 1$. The two minimas correspond to the delithiated (FePO₄) and lithiated (LiFePO₄) phases, respectively.¹ The gradient term $|\nabla c|^2$ is the penalty for the changing Li-composition field across the FePO₄ / LiFePO₄ diffuse phase boundary. The peak density field $\psi(\vec{x})$ is a time-averaged density field [31], which in its periodic state describes the coarse-grained lattice geometry of the electrode material. The term $\frac{\psi}{2}G(\nabla_c^2)\psi$ is the energy penalty resulting from the changing host-lattice structure across the diffuse phase boundary. The difference in lattice geometries between the FePO₄ / LiFePO₄ phases gives rise to a coherency strain across the phase boundary. The operator $G(\nabla_c^2)$ introduces the coupling between Li-composition $c(\vec{x})$ and host-electrode lattice symmetry $\psi(\vec{x})$. The constant γ relates the free energy normalizations of the Cahn-Hilliard and phase field crystal models, and is discussed in the appendix. The value of $r(\vec{x})$ in $f(r, \psi)$ affects the type of solutions for the peak density field $\psi(\vec{x})$. In the PFC literature, researchers have used $r(\vec{x})$ as a proxy for temperature to model glassy to non-glassy (crystalline) transition during crystallization [35, 36]. In this paper, we use $r(\vec{x})$ as a proxy for the amorphous Li-reservoir in our model. For example, with $r(\vec{x}) = -0.2$, $\psi(\vec{x})$ is a constant at equilibrium and Eq. 1 models an amorphous state. While for $r(\vec{x}) = +0.2$, $\psi(\vec{x})$ has a periodic wave-form solution at equilibrium that describes a crystalline state for the electrode material. The value of $r(\vec{x})$ is locally defined in the coordinate space to model the electrode-reservoir system. There is a surface energy contribution resulting from the difference between the crystalline electrode and amorphous reservoir regions. In this paper, the CH-PFC model does not account for the surface energy term. This surface energy contribution is important to investigate the wetting effects on phase transitions [37, 38] and is a subject of future study.

The Li-composition field is coupled to the electrode lattice geometry via the coordinate transformation coefficients of the Laplace operator ∇_c^2 . Both the FePO₄ (FP) and LiFePO₄ (LFP) lattices have an orthorhombic symmetry. There are two independent variables, α and β , which control FP / LFP lattice transformation. The variables, α and β , interpolate the lattice parameters as a function of the composition field, $\alpha(c) = \alpha_{FP} + (\alpha_{LFP} - \alpha_{FP})c$ and $\beta(c) = \beta_{FP} + (\beta_{LFP} - \beta_{FP})c$. Here, $(\alpha_{FP}, \beta_{FP})$ and $(\alpha_{LFP}, \beta_{LFP})$ correspond to the geometric measurements of FePO₄ and LiFePO₄ lattices from Table 1. With Li-composition $c = 0$ and $c = 1$, the transformation coefficients correspond to the lattice parameters of FePO₄ and LiFePO₄ respectively. The Li-composition across the diffuse phase boundary is a function $c(\vec{x})$ and the lattice is transformed according to $\alpha(c(\vec{x}))$ and $\beta(c(\vec{x}))$. The width of the diffuse

¹The X in Li_XFePO₄ and $c(\vec{x})$ are related by normalization coefficients that rescale the double well potential described by $g(c)$.

	$a_2(\text{\AA})$	$a_3(\text{\AA})$	$\alpha = \frac{a_2}{a_0}$	$\beta = \frac{a_3}{a_0}$
FePO ₄ (FP)	9.821	$a_0 = 4.788$	2.0512	1
LiFePO ₄ (LFP)	10.334	4.693	2.1583	0.9802

Table 1: A list of lattice parameters (a_2, a_3) for FePO₄ and LiFePO₄ used in the CH-PFC simulations [39]. The variable α, β are calculated using $a_0 = a_3(\text{FePO}_4) = 4.788\text{\AA}$ as reference. These coefficients describe rectangular geometries of FePO₄ and LiFePO₄ lattices at $c = 0$ and $c = 1$ respectively.

phase boundary $c(\vec{x})$ is numerically calibrated such that it spans over ~ 4 lattice spacings described by $\psi(\vec{x})$.

The time-dependent equations in the model are the Cahn-Hilliard equation for Li-diffusion:

$$\frac{\partial c}{\partial \tau} = \nabla^2 \frac{\delta \mathcal{F}}{\delta c}, \quad (2)$$

and the elastic-relaxation equation for the host lattice structure:

$$\frac{\partial \psi}{\partial n} = -\frac{\delta \mathcal{F}}{\delta \psi} + \frac{1}{L^2} \int \frac{\delta \mathcal{F}}{\delta \psi} d\vec{x}. \quad (3)$$

In Eqs. 2 – 3, we assume that the elastic relaxation (equilibrating the peak density field) is infinitely faster than the evolution of the composition field. Consequently, we model the equilibrium lattice arrangements by maintaining $\frac{\delta \mathcal{F}}{\delta \psi} \approx 0$ throughout the phase transition. The CH-PFC model is solved using an Euler discretization scheme in a 2D finite-difference framework. The computational grids have spacings of $\delta x = \delta y = \frac{4\pi}{q_0 6\sqrt{3}}$ and have periodic boundary conditions.² At each grid point the values of the composition field $c(\vec{x})$, the peak density field $\psi(\vec{x})$, and the constant $r(\vec{x})$ are represented in discrete form, as c_{ij} , ψ_{ij} and r_{ij} respectively. The time-derivative in Eq. 2 is iterated at regular time intervals of $\Delta\tau = 1$. At each time step, the composition field $c_{ij}(\tau)$ is used to update the lattice transformation coefficients, $\alpha(c_{ij}(\tau))$ and $\beta(c_{ij}(\tau))$. The coupled Laplacian ∇_c^2 is next updated and the equilibrium lattice arrangements ψ_{ij} are computed following Eq. 3. This general numerical procedure produces microstructural evolution and phase transitions.

Application to electrode microstructures

In this section, we model a representative electrode-reservoir system. The system comprises a polycrystalline FePO₄ electrode particle surrounded by an amorphous Li-reservoir. We compute

²The length scale of the CH-PFC model is $\frac{1}{q_0}$.

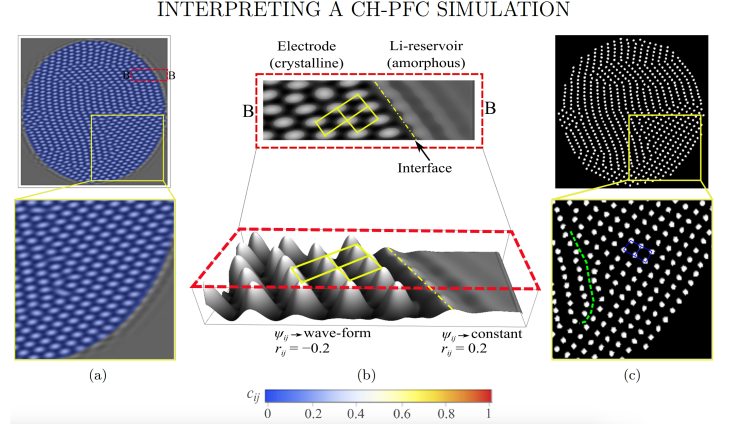


Figure 1: (a) A CH-PFC simulation of a polycrystalline FePO₄ electrode particle surrounded by an amorphous-Li-reservoir. The inset box (below) shows the host lattice points (ellipsoidal peaks) describing the FePO₄ lattice motif. The color bar indicates Li-composition c_{ij} in the electrode's interstitial sites. (b) An enlarged image of the electrode lattice symmetry is shown in the inset box BB. In the electrode region, the peak density field ψ_{ij} has a wave form where the coordination symmetry of ellipsoidal peaks represent an FePO₄ lattice. In the Li-reservoir region, ψ_{ij} is a constant and describes an amorphous state. At the electrode-reservoir interface, ψ_{ij} changes as a function of r_{ij} according to Eq. 1. (c) "Peak marker image" illustrating the centroids of the ellipsoidal peaks described by ψ_{ij} (in Fig. 1a). The inset box highlights the lattice structure (solid-blue lines) and grain boundaries (dashed-green lines) in the FePO₄ electrode. Details on the crystallographic features of the polycrystalline electrode are shown in Fig. 2.

an electrochemical cycle by inserting/extracting Li-ions into interstitial sites of the FePO₄ lattice structure. Here, we study how lattices distort across a diffuse phase-boundary, and investigate grain-boundary migration.

Electrode-reservoir system

A circular electrode of diameter $d = 290\delta x$ is modeled on a periodic grid of size $300\delta x \times 300\delta y$. The electrode is surrounded by a reservoir-region, see Fig. 1a. On the computation grid r_{ij} is locally defined to model a crystalline-region for the electrode ($r_{ij} = -0.2$) and an amorphous-region for the reservoir ($r_{ij} = 0.2$). A homogeneous composition $c_{ij} = 0$ is described on the computation grid. The transformation coefficients define the coarse-grained bond lengths and bond angles of the FePO₄ lattice geometry (see Table 1) as inputs to the CH-PFC simulation. At the initial state of the computation, a random peak density field value, $-0.1 \leq \psi_{ij} \leq 0.5$, is assigned at each grid point. Using Eq. 3, the peak density field for the electrode-reservoir system is computed. The peak density field, in the electrode region, nucleates into FePO₄ crystallites with different orientations. The initial condition with $-0.1 \leq \psi_{ij} \leq 0.5$ allows grains to evolve independently

and form a polycrystalline electrode as shown in Fig. 1a.

In Fig. 1(a-b), the peak density field ψ_{ij} has a wave-form in the electrode region and represents the FePO_4 lattice motif, see inset-box. The composition field for Li interstitials is $c_{ij} = 0$. In the reservoir region, ψ_{ij} is a constant and represents an amorphous state. At the electrode-reservoir interface, fading bands of the peak density field are observed, see inset box in Fig. 1b. These bands show a gradual change in ψ_{ij} , from its periodic wave-form in the crystalline electrode, to a constant value in the amorphous reservoir. This change in ψ_{ij} results from the abrupt change of r_{ij} values modeled across the electrode-reservoir interface. In this paper, the fading bands of ψ_{ij} represent the amorphous phase gradually taking on a crystalline character.

In Fig. 1a the peaks are of ellipsoidal shape. This shape results from the coordinate transformation coefficients in the Laplace operator ∇_c^2 , which shears the peaks anisotropically. Fig. 1a shows multiple grain boundaries in the FePO_4 electrode particle. The peaks at the grain boundaries, appear smeared and deviate from the conventional ellipsoidal shape. We interpret this smearing of peaks as a coarse-grained lattice-structure distortion, which maintains coherency between neighboring grains.

The centroids of the ellipsoidal peaks describe the rectangular coordination of the FePO_4 lattice. To highlight this symmetry, we substitute the ellipsoidal peaks with a Gaussian distribution – we refer to this image as a “peak marker image”, see Fig. 1c. Here, the centroids of the peaks, (x_0, y_0) are identified, and a 2D Gaussian distribution, $g(x, y) = \frac{2}{\pi} \exp[-2\{(x - x_0)^2 - (y - y_0)^2\}]$ is modeled around each centroid. In Fig. 1c, these Gaussian distributions are shown by white solid dots. The fading bands of ψ_{ij} at the electrode-reservoir interface are removed in the peak marker image. The FePO_4 lattice structure and a representative grain boundary are traced by solid blue and dashed green lines respectively, see the inset box in Fig. 1c. Fig. 2 highlights the crystallographic features in the FePO_4 electrode particle. Note, the peak-positions in Fig. 1c does not correspond to the atomic sites. The arrangement of peaks illustrates the coarse-grained lattice-symmetry of the electrode particle. The grain boundaries arise from the coarse-grained lattice-distortions in the underlying atomic arrangements. Further details on the interpretation of the coarse-grained lattices in CH-PFC simulations is provided in the appendix of Ref. [30].

In Fig. 2, we identify four representative crystallographic features ‘A-D’ of the FePO_4 electrode particle (simulated in Fig. 1a). These crystallographic features arise naturally from computing the time derivative of ψ_{ij} in Eq. 3. Label ‘A’, highlighted by the green and blue crystallographic planes, marks a coherent interface. These coherent grain boundaries are commonly observed in our CH-PFC simulations. Label ‘B’ marks three grain boundaries that intersect to form a triple junction. The dihedral angle(s) between these grain boundaries influence(s) the migration of the grain boundary system. For example, if the grain boundaries are equally inclined at 120° , the triple-junction tends not to move. However, if the grain boundaries are unequally inclined, they drag the triple-junction towards the centre of a single grain. This “triple-junction drag-effect” is discussed in the next section (Electrochemical cycle). Labels ‘C’ and ‘D’ indicate, respectively, the high-angle and low-

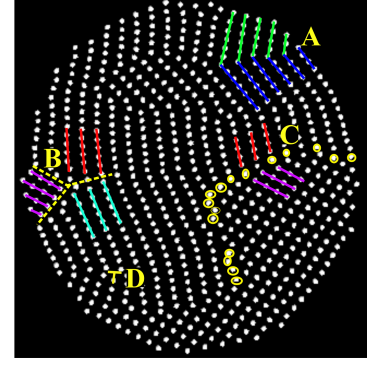


Figure 2: An illustration of the crystallographic features in the polycrystalline FePO_4 electrode particle (shown in Fig. 1a). (A) A coherent grain boundary with a perfect match between the crystallographic planes. (B) A triple junction formed at the intersection of three grains. The dashed yellow lines highlight the grain boundary system. (C) A chain of defects, highlighted by yellow circles, form a high angle grain boundary ($> 15^\circ$). (D) An edge-dislocation defect illustrated by a ‘T’.

angle grain boundaries in the electrode particle. Grain boundaries with larger misorientation angle $> 15^\circ$ are incoherent and have a chain of edge-dislocations as shown by label ‘C’. Grain boundaries with a misorientation angle less than 15° tend to be more coherent and have fewer defects. For example, in Fig. 2, ‘D’ shows an edge-dislocation defect that is highlighted by a pair of short yellow lines. We next lithiate and delithiate this polycrystalline electrode particle to investigate how its crystallographic features evolve during an electrochemical cycle.

Electrochemical cycle

In the following simulations, we specify a chemical potential to the Li-reservoir, which is held fixed during the lithiation / delithiation cycle. This boundary condition is a proxy for our assumption that the Li-diffusion rate is greater in the reservoir than in the electrode particle. For example, we specify the Li-reservoir with $c_{ij} = 1$ that is fixed during lithiation. The composition gradient between the FePO_4 electrode ($c_{ij} = 0$) and the Li-reservoir creates a boundary condition, which causes Li-ions to diffuse into the electrode; see Fig. 3.

Fig. 3a is a CH-PFC simulation of a partially lithiated electrode particle. Fig. 3b shows the composition variation across the diffuse FePO_4 / LiFePO_4 phase boundary. The inset image in Fig. 3c illustrates the coarse-grained lattice distortions across the phase boundary. This phase boundary is analogous to the ‘staging structure’ observed in some intercalation compounds [32]. For example, the interfacial region between the FePO_4 and LiFePO_4 phases has non-stoichiometric Li-composition (i.e., Li_xFePO_4 where $0 < x < 1$).

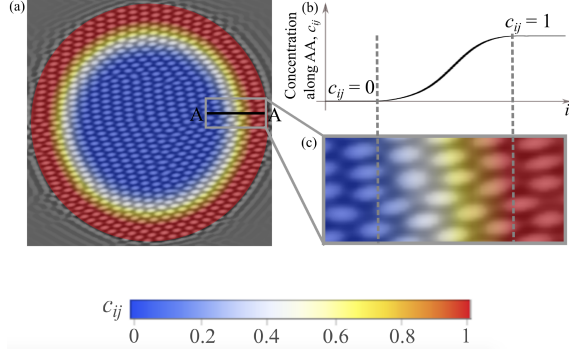


Figure 3: (a) Lattice arrangements in a partially lithiated FePO_4 electrode particle. The color bar illustrates Li-composition in FePO_4 (blue $c_{ij} = 0$) and LiFePO_4 (red $c_{ij} = 1$) phases. A diffuse phase boundary (yellow $0 < c_{ij} < 1$) separates the two phases. (b) The distribution of Li-composition field c_{ij} across a diffuse phase boundary (for example, along AA). (c) The peak density field ψ_{ij} across the diffuse phase-boundary. The width of the diffuse interface (highlighted by vertical dashed-lines) is numerically calibrated to span over ~ 4 lattice points.

Lithiation

Fig. 4 shows the temporal evolution of the electrode microstructure during lithiation, as a function of c_{ij} and ψ_{ij} . The subfigures in row 1 illustrate the lattice arrangements in the host-electrode particle as a function of the interstitial Li-composition. The corresponding peak marker images of the host-electrode are shown in row 2. The approximate positions of three representative grain boundaries ‘A–C’ are marked on the electrode’s lattice structure. The positions and orientations of these grain boundaries are tracked during the electrochemical cycle. Subfigures in row 3 are the distortion maps that indicate the absolute difference in electrode’s peak positions with a reference state. That is, the host-electrode lattices undergo displacive transformations during an electrochemical cycle, which are tracked on the distortion maps. In the lithiation cycle, the reference state is the initial FePO_4 particle shown in Fig. 4a. The distortion at each grid point is calculated as $\delta_{ij} = \frac{\|x_{ij}(\tau) - x_{ij}(\tau=0)\|}{\delta_0}$. Here, $x_{ij}(\tau)$ is the discrete representation of the peak position at time τ . The $\|\dots\|$ represents the euclidean distance between a peak position at time τ with reference to its initial position at $\tau = 0$ in Fig. 4a. The normalizing constant, $\delta_0 = \beta_{\text{FP}} = \frac{4\pi}{q_0\sqrt{3}}$, is the equilibrium separation between two adjacent Gaussian-peaks. The distortion maps illustrate the lattice deformations in the host-electrode particle that are induced by Li-diffusion.

As the Li-intercalation wave propagates into the electrode as in Fig. 4a – 4c, the shape and size of grains ‘A–C’ change. In the grain-boundary system ‘A’, the smallest grain ‘a₁’ near the electrode edge shrinks until it disappears in Fig. 4d. This relieves the inhomogeneous strain field in the larger grain ‘A’. The larger grain ‘A’ grows in size during lithiation. The grain boundary ‘C’ tends to move towards its center of curvature. This is consistent with the motion by curvature observed in material microstructures [40–42]. In Fig. 4b row 3, lattice distortions $\delta_{ij} \approx 0.12$ are observed in the lithiated phase of the electrode particle. We interpret

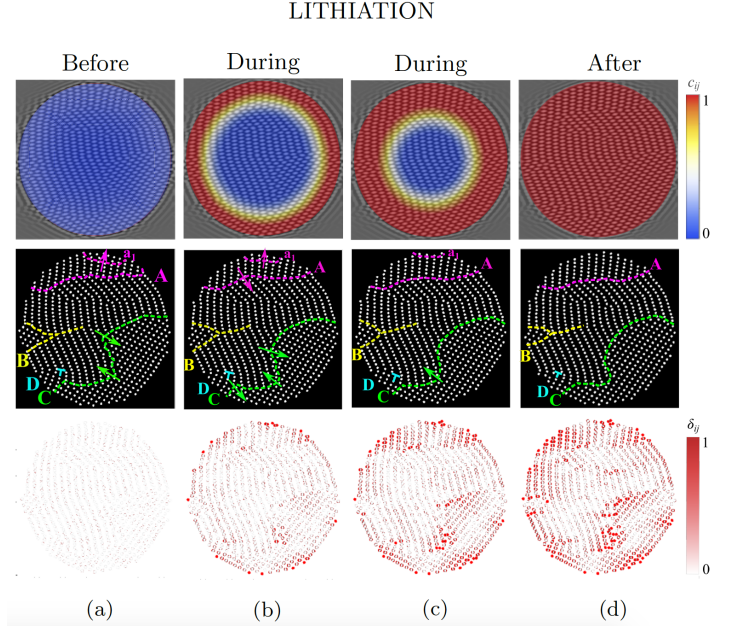


Figure 4: (a-d): Lithiation of the polycrystalline FePO_4 electrode particle. Starting from an initial FePO_4 phase (a), Li-ions intercalate into the electrode particle (b-c). A LiFePO_4 phase is formed at the end of lithiation (d). The subfigures in row 1 show the temporal evolution of the Li-composition c_{ij} in the electrode particle. The subfigures on row 2 show the structural transformation of lattices in the host-electrode during lithiation. The labels ‘A–D’ highlight representative crystallographic features in the electrode particle. The subfigures in row 3 illustrate the distortion maps δ_{ij} corresponding to each stage of lithiation. We interpret δ_{ij} to show host lattice distortions induced from Li-intercalation.

pret that these distortions correspond with the ferroelastic lattice strains that accompany FePO_4 / LiFePO_4 phase transition. The lattice arrangements in the electrode core show negligible variation in peak positions, $\delta_{ij} \approx 0$. In Fig. 4c row 3, relatively large distortions $\delta_{ij} > 0.5$ are observed along grain boundaries in the electrode. We interpret these distortions $\delta_{ij} > 0.5$ to correspond with the grain-boundary migration. At the end of lithiation, a LiFePO_4 phase forms in the host electrode, see Fig. 4d. The distortion map in Fig. 4d row 3, indicates ferroelastic lattice strains throughout the electrode particle.

Delithiation

We next delithiate the electrode particle starting from Fig. 4d. We model the Li-reservoir with a composition field $c_{ij} = 0$, which is held fixed throughout the delithiation process. Fig. 5 shows the temporal evolution of the electrode microstructure as Li-ions are extracted from the host lattices. The subfigures in row 1 show the microstructures as a function of the interstitial Li-composition. The host-electrode lattice arrangements and distortion maps are illustrated in row 2 and row 3, respectively. Note, the distortion maps in Fig. 5 plot the absolute difference in peak positions, using the lattice arrangements in Fig. 5a as the reference.

DELITHIATION

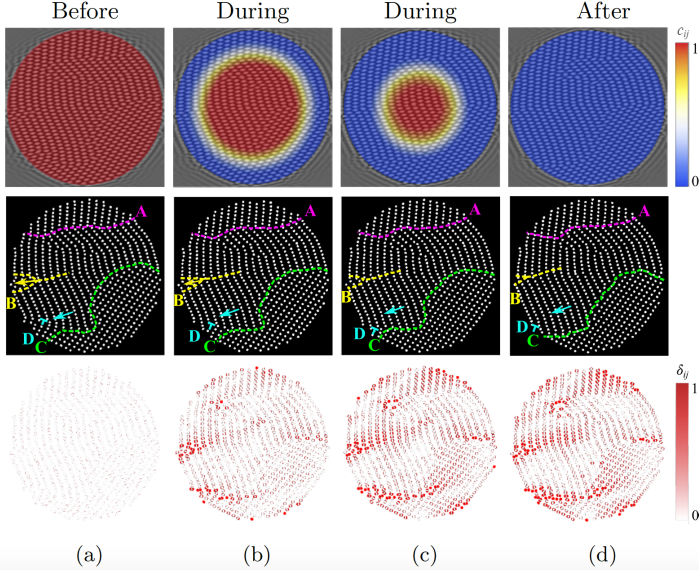


Figure 5: (a-d): Delithiation of a LiFePO_4 electrode particle. Starting from the initial LiFePO_4 phase (a), Li-ions are extracted from the electrode particle (b-c). An FePO_4 phase is formed at the end of delithiation (d). The subfigures in row 1 show the temporal evolution of Li-composition c_{ij} in the electrode particle. The subfigures on row 2 show the structural transformation of lattices in the host-electrode during delithiation. The labels ‘A–D’ highlight representative grain boundaries. The subfigures in row 3 illustrate the lattice distortion maps δ_{ij} corresponding to each stage of delithiation. The distortions in Fig. 5 are calculated as the absolute difference in peak positions using the lattice arrangements in subfigure 5a as reference.

During delithiation, LiFePO_4 lattices undergo displacive transformation to describe FePO_4 lattice structure. Grain ‘B’ shrinks in size and disappears at the end of delithiation (Fig. 5, row 2). The grain-boundary system ‘B’, with unequal dihedral angles, drags the triple junction as shown in Fig. 5(a-d). Note that grains ‘a₁’ and ‘B’ are of comparable sizes. However, Fig. 4 – 5 qualitatively illustrates that grain ‘a₁’ shrinks faster than grain ‘B’. We interpret that the slow migration of the grain-boundary system ‘B’ results from the triple-junction drag effect. This drag effect has been observed by Shvindlerman et al. [43, 44] and has also been reported in electrode microstructures [45]. The edge dislocation ‘D’ moves towards the electrode particle’s surface during delithiation. Extraction of Li-ions from the host-electrode induces this dislocation movement. In Fig. 5d, the electrode particle is returned to the FePO_4 phase at the end of delithiation. The electrode particle in Fig. 5d has a different lattice-arrangement from its initial state in Fig. 4a. Similar dislocation dynamics have been observed in experiments [46], [47]. For example, Ulvestad et al. [46] reported that an applied current induced dislocation movement in an intercalation cathode particle ($\text{LiNi}_{0.5}\text{Mn}_{1.5}\text{O}_4$). The dislocation was sta-

NON-CYCLED ELECTRODE

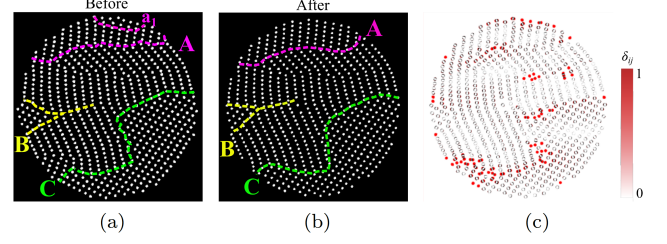


Figure 6: Lattice rearrangements in the non-cycled polycrystalline electrode particle. The electrode-reservoir system is modeled with a homogeneous Li-composition $c_{ij} = 0$, and computed for the same time (τ_{total}) and temperature as in Figs. 4 – 5. The host-electrode lattice arrangements (a) before $\tau/\tau_{\text{total}} = 0$, and (b) after $\tau/\tau_{\text{total}} = 1$ the non-cycled grain growth. (c) The lattice distortion map δ_{ij} calculated as the absolute difference in peak positions between the ‘before’ and ‘after’ stages of the non-cycled electrode. The distortion map illustrates lattice rearrangements near grain-boundaries.

ble at room temperature and migrated to the particle surface under an electrical load [46]. In hydrogen-palladium nanocubes [47], Narayan et al. [47] reported that the diffusion of hydrogen-atoms in host-palladium particle mobilized its edge-dislocations.

In Figs. 4 – 5 grain-boundary migration ($\delta_{ij} \approx 1$) is primarily observed in electrode regions that are swept across by the Li-intercalation wave. We hypothesize that the grain-boundary migration is induced by Li-intercalation [11, 12]. That is, insertion or extraction of Li-ions from the host lattice is accompanied by a change in the host-lattice geometry. The difference in lattice parameters between the lithiated and delithiated phases generates lattice misfit strains. This lattice misfit results in a stored elastic energy, which acts as an additional driving force for grain-boundary migration beyond its curvature [11, 12]. We next test this hypothesis by simulating grain growth in the same electrode particle (Fig. 4a), without Li-intercalation. In this non-cycled electrode particle, grain growth has no additional driving force.

Non-cycled electrode

We model the electrode-reservoir system as shown in Fig. 4a. We define a homogeneous Li-composition field $c_{ij} = 0$ on the computation grid. We compute the time evolution of lattice arrangements in the electrode following Eq. 3 [30]. We iterate Eq. 3 for the same computation time τ_{total} as required to electrochemically cycle the electrode in Figs. 4 – 5. We refer to this computation as the “non-cycled grain growth” of the electrode particle.

Fig. 6a and Fig. 6b respectively illustrate the lattice arrangements in the host-electrode particle before and after the computation. The lattice distortion map in Fig. 6c illustrates structural rearrangements in the host electrode particle. Lattice distortions $\delta_{ij} \approx 1$ are primarily observed along grain boundaries with a non-zero radius of curvature. This suggests that grain-boundary mi-

gration in Fig. 6b – 6c is curvature-driven. These migrations are however small in comparison to Figs. 4 – 5. For example in Figs. 4 – 5, the grain ‘B’ shrinks at the end of lithiation / delithiation cycles. However in Fig. 6, with no Li-intercalation, grain ‘B’ only slightly reduces in size. Similarly grains ‘A’ and ‘C’ show a small variation in their shape and size. Fig. 6 is consistent with our hypothesis that Li-intercalation assists (or accelerates) grain-boundary migration.

Discussion

We compare grain growth in electrode particles that were electrochemically cycled and non-cycled in Fig. 7(a-b), respectively. The schematics, at the top of the plots show Li-composition c in the electrode particle at each computation time step, τ/τ_{total} . Note, τ_{total} is the computation time required for one electrochemical cycle. The grain size $\frac{\bar{A}}{\mathcal{A}_e}$ is normalized by the electrode area \mathcal{A}_e . Fig. 7a illustrates that the mean grain-size, averaged over all the grains in the electrode particle, grows by 11% upon electrochemical cycling. Smaller grains ‘A’ and ‘B’ shrink, and the larger grain ‘C’ has an approximately constant grain-size throughout the electrochemical cycle.

In Fig. 7b, the mean grain-size grows by $\sim 2\%$ in the non-cycled electrode particle. The grain sizes of A, B and C are approximately constant throughout the computation. In the absence of Li-intercalation, the grain-boundary migration is curvature-driven. In Fig. 7b, the grain growth (mean) follows a relationship of the form $\frac{\bar{A}}{\mathcal{A}_e} \approx g_0 + g\left(\frac{\tau}{\tau_{\text{total}}}\right)^n$, where $n \approx 0.5$.³ This is consistent with the curvature-driven grain growth observed in experiments [40]. In Fig. 7a the grain growth follows a similar relationship, however, with the exponent $n > 0.5$. This suggests an accelerated grain growth (mean) in Fig. 7a. Fig. 7(a-b) indicates that Li-intercalation accelerates grain-boundary migration in the electrode particle. This observation is consistent with the diffusion-induced grain-boundary migration discussed in the works of Handwerker et al. [11, 12].

We find the work of Bates et al. [6] on sputter-deposited thin film cathodes, as the closest experimental comparison to the diffusion-induced grain growth effect suggested by our present work. Bates et al. [6] described the cathodes as undergoing grain growth during electrochemical cycling at near-ambient temperature [6]. Another related phenomena are the observations of accelerated grain growth in fluorite structure solid electrolytes at elevated temperature. In these solid electrolytes electrical load has been observed to accelerate grain growth kinetics [7, 9]. We suggest that systematic experimental investigation of battery electrodes after extensive cycling will reveal lattice-strain-induced grain growth as observed in this paper.

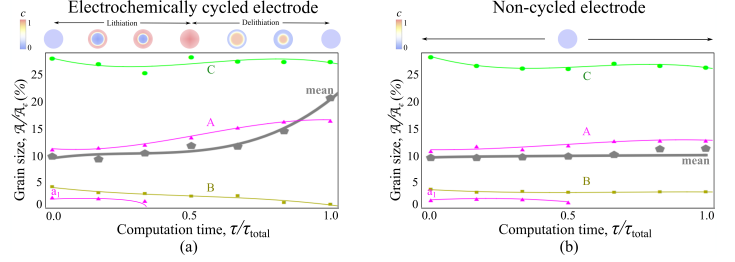


Figure 7: Grain growth \bar{A}/\mathcal{A}_e in an electrode particle when it is (a) electrochemically cycled and (b) non-cycled. The schematics above the plots illustrate Li-composition c in the electrode particle at the corresponding computation times.

Fig. 8(a-c) shows the grain-size distributions for the electrochemically cycled and non-cycled electrode particle. Histograms of grain-size distributions at three stages of the CH-PFC computation, namely $\tau/\tau_{\text{total}} = 0, 0.5$ and 1, are plotted. They show the mean grain-size (\bar{A}/\mathcal{A}_e) and number of grains (frequency) in the electrode-particle at each stage. The histograms in Fig. 8(a-c) show a good fit to the log-normal size distributions, which are observed in experiments [7, 9, 48]. In the electrochemically cycled electrode, the variance (width) of the grain-size distribution decreases upon Li-intercalation. In the non-cycled electrode particle, see Fig. 8(right), the variance of its size-distribution is approximately constant throughout the computation. These results suggest that smaller grains in the electrochemically cycled electrode particle, with $\log(\bar{A}/\bar{A}) < -0.5$, disappear at the expense of bigger grains. Electrode particles with enhanced grain sizes tend to be less tough in comparison to samples with smaller grains [3, 5]. Fig. 8 suggests that Li-intercalation is an additional process that affects the mechanical reliability in batteries.

We next discuss a few issues that arise in interpreting the CH-PFC simulations in Figs. 4 to 6. For example, the electrode-particle volume (or area) is held constant during the computation. However, the number density of peaks in the electrode-particle is not conserved.⁴ That is, the peaks move in/out at the electrode-reservoir interface to accommodate for the lattice-area change during phase transformation. This ‘‘artificial boundary condition’’ applied to the electrode-reservoir interface does not impose volume-confinement stresses on the electrode-particle. In future works, we propose to introduce numerical correction terms [49] to Eq. (6) to conserve the total number of peaks in the electrode region.

Another issue is related to the isotropic Li-diffusion in the electrode-particle. In olivine materials, such as FePO_4 , Li-ions preferentially diffuse through the host’s one-dimensional channels [50]. In previous continuum models [13, 14, 16, 26], researchers have modeled this preferential diffusion by using an anisotropic diffusion coefficient. In these methods the crystallographic planes of FePO_4 were typically oriented relative to a cartesian basis. The anisotropic Li-diffusion was modeled with reference to the coordinate axes. In the CH-PFC model, however, the crystallographic planes

³ $g_0 = 9.23, g = 1.12$

⁴Please note, the addition/removal of peaks does not affect the coarse-grained lattice structure described by ψ_{ij} [30].

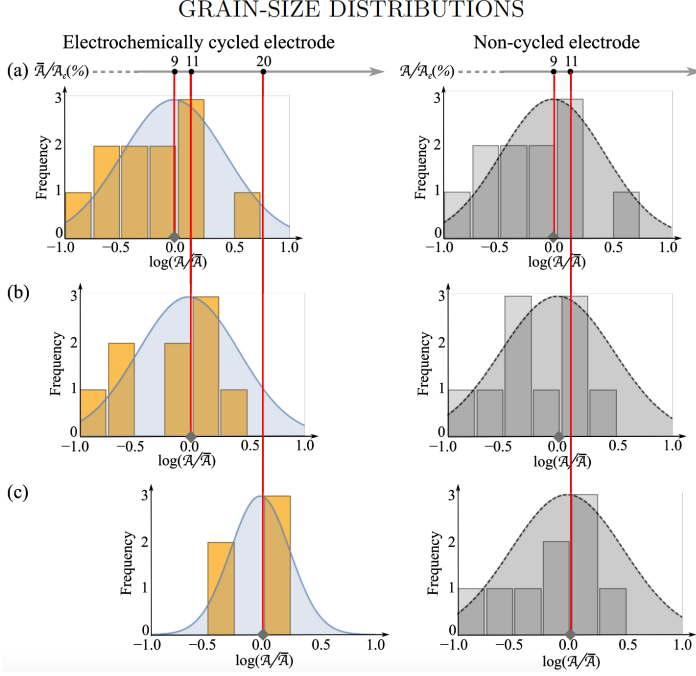


Figure 8: Grain-size distributions in the electrochemically cycled (left) and non-cycled (right) electrode particle. The subfigures correspond to the electrode microstructures at (a) $\tau/\tau_{\text{total}} = 0$ (b) $\tau/\tau_{\text{total}} = 0.5$ and (c) $\tau/\tau_{\text{total}} = 1$. The position of the red lines corresponds to the mean grain-size values on the vertical axes in Fig. 7. The grain-size distributions indicate that electrochemical cycling accelerates grain-growth in the electrode particle.

of FePO_4 / LiFePO_4 are a natural outcome in the simulations. We assume an isotropic bulk-diffusion coefficient D in Eq. (2) to model lithiation/delithiation; see Figs. 4 and 5. We do, however, see anisotropy in Li-diffusion arising from the coordinate-transformation-coefficients in the coupled term $\nabla^2 \gamma \frac{\psi}{2} \frac{\partial G(\nabla_c^2)}{\partial c} \psi$.⁵ This contribution is negligible as a result of the diffuse width (~ 4 coarse-grained lattices) of the phase boundary. The value of the constant γ also influences the anisotropy contribution from the coupled term. In this paper we set $\gamma = \frac{\lambda^2 q_0^5}{u F_0} = 1$ for computational expediency. That is, the energy contribution from the PFC equation is negligible (i.e., $\sim 10^{-19} F_0$). Consequently, the isotropic diffusion of the Li-intercalation wave is relatively unaffected by the anisotropy in ψ_{ij} . However, if γ is large the effects from material crystallography and lattice defects are expected to appear in the simulations.

Overall, the CH-PFC methods has three specific advantages in modeling phase transitions in intercalation electrodes: First, the CH-PFC simulations provide qualitative insights on phenomenological mechanisms across different length and time scales. For example, the simulations describe Li-diffusion at a continuum scale and grain-boundary migration at an atomistic scale. Second, the

crystallographic planes of FP/LFP lattices in the electrode particle are an emergent phenomenon of the CH-PFC simulations [51]. The crystallographic misorientations at grain boundaries follow naturally from the simulations. Third, in the CH-PFC model the coarse-grained lattices distort independently as a function of the interstitial Li-composition. That is, lattice geometries are different in the lithiated and delithiated phases. This difference generates coherency strains across the diffuse phase boundary. The coherency strains in the CH-PFC simulations are a natural outcome resulting from the different lattice geometries, and are not modeled as an approximation from the composition field [13, 14, 17, 26]. This results in inhomogeneous strains across grain boundaries and phase boundaries in a polycrystalline electrode.

Summary

We demonstrate that Li-diffusion accelerates grain growth in intercalation compounds using FePO_4 / LiFePO_4 as a model system. We present an application of the Cahn-Hilliard – phase-field-crystal methods to model phase transitions in a polycrystalline FePO_4 electrode particle. This modeling approach illustrates multiscale interactions between Li-diffusion (continuum parameter) and structural transformations of host-lattices (atomistic) during an electrochemical cycle. While grain growth from cyclic intercalation has not been experimentally confirmed, our study suggests that volume changes in electrode upon Li-intercalation accelerates grain growth. The results qualitatively describe phenomenological mechanisms in intercalation electrodes, such as edge-dislocation movement and the triple-junction-drag effect. The CH-PFC model could be applied to investigate chemo-mechanically coupled problems that involve solute-induced phase transitions.

Acknowledgements

The authors gratefully acknowledge the support by the grant DE-SC0002633 funded by the U.S. Department of Energy, Office of Science, in carrying out this work. A. Renuka Balakrishna also acknowledges the support of the Lindemann postdoctoral fellowship.

Appendix

A.1 CH-PFC model details

In this section we provide a brief explanation of the CH-PFC model. For the derivation of the CH-PFC model please refer to Ref. [30]. The CH-PFC model describes the total free energy F , as a function of the composition field \bar{c} and the peak density field ϕ :

$$\begin{aligned} F &= \int \{g(\bar{c}) + \kappa |\nabla \bar{c}|^2 + f(\phi) + \frac{\phi}{2} G(\nabla_c^2) \phi\} d\vec{r} \\ &= \int \{RT[\bar{c} \ln(\bar{c}) + (1 - \bar{c}) \ln(1 - \bar{c})] + \Omega \bar{c}(1 - \bar{c}) \\ &\quad + \kappa |\nabla \bar{c}|^2 + \frac{\phi}{2} (a \Delta T_0 + \lambda (q_0^2 + \nabla_c^2)^2) \phi + u \frac{\phi^4}{4}\} d\vec{r}. \end{aligned} \quad (4)$$

⁵Please see Eq. (8) in the appendix.

Eq. 4 in its normalized form is:

$$\begin{aligned}\mathcal{F} &= \frac{F}{F_0} = \int \{g(c) + |\nabla c|^2 + f(\psi) + \frac{\psi}{2} G(\nabla_c^2) \psi\} d\vec{x} \\ &= \int \{c \ln(c) + (1-c) \ln(1-c) + \Omega_0 c(1-c) \\ &\quad + |\nabla c|^2 + \gamma \left(\frac{\psi}{2} (r + (1 + \nabla_c^2)^2) \psi + \frac{\psi^4}{4} \right)\} d\vec{x},\end{aligned}\quad (5)$$

where $c = \frac{\bar{c}_a - \bar{c}}{\bar{c}_a - \bar{c}_b}$, and $\psi = \phi \sqrt{\frac{u}{\lambda q_0^4}}$. The gradient energy coefficient $\kappa = \frac{F_0}{(\bar{c}_a - \bar{c}_b)^2} \left(\frac{16\pi\xi}{q_0\sqrt{3}} \right)^2$, is numerically calibrated such that the width of the diffuse composition interface spans over ~ 4 lattice spacings described by the peak density field, ψ . Note, $\frac{1}{q_0}$ is the length scale of the CH-PFC model and ξ is the scale factor that coarse-grains the lattice units. The form of Eq. 4-5 is similar to that in the work of Renuka-Balakrishna and Carter [30] where detailed explanations of the specific terms, constants ($\bar{c}_a, \bar{c}_b, \lambda, q_0, u, \xi$) and normalizations are provided. Note, the coefficients in the regular solution model are the same as in Ref. [14]. In Eq. 5, $g(c)$ and $f(\psi)$ describe the homogeneous energy contributions from the Cahn-Hilliard and phase-field-crystal equations respectively. The composition gradient-energy is given by $|\nabla c|^2$. The parameter r , controls the second-order phase transition of the PFC model. The constant $\gamma = \frac{\lambda^2 q_0^5}{u F_0}$ relates the free energy normalizations of the Cahn-Hilliard and the PFC model. In this paper we set $\gamma = 1$ and $\xi = 1$ for computational expediency.

The Cahn-Hilliard and the phase-field-crystal models are coupled via the operator $G(\nabla_c^2) = (1 + \nabla_c^2)^2$. The composition field is coupled to the lattice symmetry via the Laplace operator:

$$\nabla_c^2 = \xi^2 ((A_{11}^2 + A_{12}^2) \frac{\partial}{\partial x^2} + A_{22}^2 \frac{\partial}{\partial y^2} + 2A_{12}A_{22} \frac{\partial}{\partial x \partial y}). \quad (6)$$

Here, A_{kl} are the elements of the transformation matrix and are described as functions of the composition field:

$$\mathbf{A}(c) = \begin{bmatrix} \alpha(c) & \frac{-\alpha(c)}{\sqrt{3}} \\ 0 & \frac{2\beta(c)}{\sqrt{3}} \end{bmatrix}. \quad (7)$$

The matrix $\mathbf{A}(c)$, describes affine lattice transformations using hexagonal symmetry as the reference structure. The transformation coefficients in Eq. 7 transform a hexagonal symmetry (of unit size) to rectangular geometries of FePO_4 (with $c = 0$) and LiFePO_4 (with $c = 1$) in 2D [39], see Fig. 9. The transformation coefficients are given by $\alpha(c) = \alpha_{\text{FP}} + (\alpha_{\text{LFP}} - \alpha_{\text{FP}})c$ and $\beta(c) = \beta_{\text{FP}} + (\beta_{\text{LFP}} - \beta_{\text{FP}})c$. The values of $(\alpha_{\text{FP}}, \beta_{\text{FP}})$ and $(\alpha_{\text{LFP}}, \beta_{\text{LFP}})$ correspond to FePO_4 and LiFePO_4 lattices and are obtained from Table 1. During electrochemical cycling, the composition field in a two-phase FP/LFP microstructure is a function $c(\vec{x})$. The lattices in this microstructure are transformed according to $\mathbf{A}(c(\vec{x}))$.

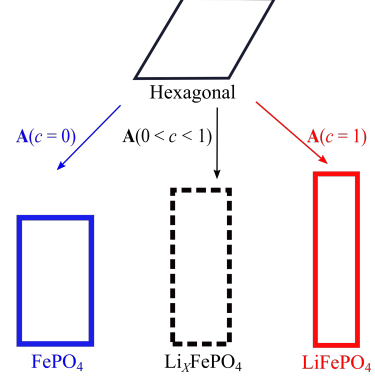


Figure 9: Schematic representations of the coupling between lattice symmetry and composition field in the CH-PFC model. The transformation matrix $\mathbf{A}(c)$, is described as a function of the composition field, c . For $c = 0$, $\mathbf{A}(c)$ deforms a hexagonal symmetry to rectangular FePO_4 lattice (in blue, far left). For $c = 1$, $\mathbf{A}(c)$ describes the lattice motif of LiFePO_4 (in red, far-right). For $0 < c < 1$, intermediate lattice geometries of the interphase Li_xFePO_4 (dashed box) is modeled.

Next, we list the detailed equations of motion used in the CH-PFC model. The evolution of the composition field follows a generalized Cahn-Hilliard equation:

$$\begin{aligned}\frac{\partial c}{\partial \tau} &= \nabla^2 \frac{\delta \mathcal{F}}{\delta c} \\ &= \nabla^2 \left(\frac{\partial g(c)}{\partial c} - \nabla^2 c + \gamma \frac{\psi}{2} \frac{\partial (\nabla_c^4 + 2\nabla_c^2)}{\partial c} \psi \right).\end{aligned}\quad (8)$$

where, $\gamma = 1$ and τ is the dimensionless time variable $\tau = t \frac{D}{L^2}$. Here, D is the isotropic diffusion coefficient and L is the size of the computational grid. Eq. (8) introduces two Laplace operators, ∇^2 and ∇_c^2 , respectively. The Laplacian $\nabla^2 = \frac{\partial^2}{\partial x^2} + \frac{\partial^2}{\partial y^2}$ describes an isotropic Li-diffusion. We do, however, see anisotropy in $\frac{\partial c}{\partial \tau}$ because of the coordinate transformation coefficients in ∇_c^2 and from grain boundaries in the host-electrode system. The coupled Laplacian ∇_c^2 computes the derivatives of the peak density field in a transformed coordinate space. The term $\nabla^2 \gamma \frac{\psi}{2} \frac{\partial (\nabla_c^4 + 2\nabla_c^2)}{\partial c} \psi$ is anisotropic and influences the Li-intercalation. This anisotropic effect is negligible in the CH-PFC simulations of this paper, because the diffuse phase boundary spans over ~ 4 lattice spacings. The lattice arrangement at each composition evolution step is computed as:

$$\begin{aligned}\frac{\partial \psi}{\partial n} &= -\frac{\delta \mathcal{F}}{\delta \psi} + \frac{1}{L^2} \int \frac{\delta \mathcal{F}}{\delta \psi} d\vec{x} \\ &= -\gamma [(r + (1 + \nabla_c^2)^2) \psi + \psi^3] \\ &\quad + \frac{1}{L^2} \int \gamma [(r + (1 + \nabla_c^2)^2) \psi + \psi^3] d\vec{x}.\end{aligned}\quad (9)$$

Here, we assume that the elastic relaxation (equilibrating the peak density field) is infinitely faster than the evolution of the composition field. Consequently, we model the equilibrium lattice arrangements by maintaining $\frac{\delta \mathcal{F}}{\delta \psi} \approx 0$ throughout the phase transition. In Eq. (9), n is a fictive time-like variable that is rapidly changing in comparison to the dimensionless time, τ . Further details on Eq. (4) – (5) can be found in Ref. [30].

A.2 Modeling lattice symmetries using PFC methods

The coordinate transformation coefficients introduced in the CH-PFC model [30] resemble the lattice stretch and shear factors used in the anisotropic PFC methods [52], [53]. The stretch/shear factors deform a lattice symmetry and are used to calculate the anisotropic model coefficients. The transformation coefficients in the CH-PFC model, however, differ from the anisotropic coefficients in two ways: First, the CH-PFC model computes the Laplacian in a transformed coordinate space. The coefficients correspond to the elements of a transformation matrix, which relates lattice symmetries in 2D point groups via affine transformations. Second, the transformation coefficients are coupled to a composition field, which influences the underlying lattice symmetry of the host material.

References

- [1] Xiang, K., Xing, W., Ravnsbæk, D.B., Hong, L., Tang, M., Li, Z., Wiaderek, K.M., Borkiewicz, O.J., Chapman, K.W., Chupas, P.J. and Chiang, Y.M. (2017). Accommodating High Transformation Strains in Battery Electrodes via the Formation of Nanoscale Intermediate Phases: Operando Investigation of Olivine NaFePO₄. *Nano Letters*, 17(3), 1696-1702.
- [2] Yuan, Y., Nie, A., Odegard, G.M., Xu, R., Zhou, D., Santhanagopalan, S., He, K., Asayesh-Ardakani, H., Meng, D.D., Klie, R.F. and Johnson, C. (2015). Asynchronous crystal cell expansion during lithiation of K⁺-stabilized α -MnO₂. *Nano letters*, 15(5), 2998-3007.
- [3] Woodford, W. H., Carter, W. C., & Chiang, Y. M. (2012). Design criteria for electrochemical shock resistant battery electrodes. *Energy & Environmental Science*, 5(7), 8014-8024.
- [4] Tsai, P. C., Wen, B., Wolfman, M., Choe, M. J., Pan, M. S., Su, L., Thornton, K., Cabana, J. and Chiang, Y. M. (2018). Single-particle measurements of electrochemical kinetics in NMC and NCA cathodes for Li-ion batteries. *Energy & Environmental Science*, 11(4), 860-871.
- [5] Swallow, J. G., Woodford, W. H., McGrogan, F. P., Ferralis, N., Chiang, Y. M., & Van Vliet, K. J. (2014). Effect of electrochemical charging on elastoplastic properties and fracture toughness of Li_xCoO₂. *Journal of The Electrochemical Society*, 161(11), F3084-F3090.
- [6] Bates, J. B., Dudney, N. J., Neudecker, B., Ueda, A., & Evans, C. D. (2000). Thin-film lithium and lithium-ion batteries. *Solid State Ionics*, 135(1-4), 33-45.
- [7] Kim, S. W., Kim, S. G., Jung, J. I., Kang, S. J. L., & Chen, I. W. (2011). Enhanced Grain Boundary Mobility in Yttria-Stabilized Cubic Zirconia under an Electric Current. *Journal of the American Ceramic Society*, 94(12), 4231-4238.
- [8] Li, C. L., & Fu, Z. W. (2007). All-solid-state rechargeable thin film lithium batteries with Li_xMn₂O₄ and Li_xMn₂O₄ – 0.5 ZrO₂ cathodes. *Electrochimica acta*, 52(20), 6155-6164.
- [9] Dong, Y., Wang, H., & Chen, I. W. (2017). Electrical and hydrogen reduction enhances kinetics in doped zirconia and ceria: I. grain growth study. *Journal of the American Ceramic Society*, 100(3), 876-886.
- [10] Wang, J., Chen-Wiegart, Y. C. K., & Wang, J. (2014). In operando tracking phase transformation evolution of lithium iron phosphate with hard X-ray microscopy. *Nature Communications*, 5, 4570.
- [11] Handwerker, C. A., & Cahn, J. W. (1987). Microstructural control through diffusion-induced grain boundary migration. *MRS Online Proceedings Library Archive*, 106.
- [12] Carter, W. C., & Handwerker, C. A. (1993). Morphology of grain growth in response to diffusion induced elastic stresses: Cubic systems. *Acta metallurgica et materialia*, 41(5), 1633-1642.
- [13] Tang, M., Carter, W. C., & Cannon, R. M. (2006). Diffuse interface model for structural transitions of grain boundaries. *Physical Review B*, 73(2), 024102.
- [14] Tang, M., Huang, H. Y., Meethong, N., Kao, Y. H., Carter, W. C., & Chiang, Y. M. (2009). Model for the particle size, overpotential, and strain dependence of phase transition pathways in storage electrodes: application to nanoscale olivines. *Chemistry of Materials*, 21(8), 1557-1571.
- [15] Meethong, N., Huang, H. Y. S., Carter, W. C., & Chiang, Y. M. (2007). Size-dependent lithium miscibility gap in nanoscale Li_{1-x}FePO₄. *Electrochemical and Solid-State Letters*, 10(5), A134-A138.
- [16] Bai, P., Cogswell, D. A., & Bazant, M. Z. (2011). Suppression of phase separation in LiFePO₄ nanoparticles during battery discharge. *Nano letters*, 11(11), 4890-4896.
- [17] Cogswell, D. A., & Bazant, M. Z. (2012). Coherency strain and the kinetics of phase separation in LiFePO₄ nanoparticles. *ACS nano*, 6(3), 2215-2225.
- [18] Srinivasan, V., & Newman, J. (2004). Discharge model for the lithium iron-phosphate electrode. *Journal of the Electrochemical Society*, 151(10), A1517-A1529.
- [19] Han, B. C., Van der Ven, A., Morgan, D., & Ceder, G. (2004). Electrochemical modeling of intercalation processes with phase field models. *Electrochimica Acta*, 49(26), 4691-4699.
- [20] Moriwake, H., Kuwabara, A., Fisher, C.A., Huang, R., Hitosugi, T., Ikuhara, Y.H., Oki, H. and Ikuhara, Y. (2013). First-Principles Calculations of Lithium-Ion Migration at a Coherent Grain Boundary in a Cathode Material, LiCoO₂. *Advanced Materials*, 25(4), 618-622.
- [21] Mo, Y., Ong, S. P., & Ceder, G. (2011). First principles study of the Li₁₀GeP₂S₁₂ lithium super ionic conductor material. *Chemistry of Materials*, 24(1), 15-17.
- [22] Zhao, J., Buldum, A., Han, J., & Lu, J. P. (2000). First-principles study of Li-intercalated carbon nanotube ropes. *Physical review letters*, 85(8), 1706.

- [23] Fisher, C. A., & Islam, M. S. (2008). Surface structures and crystal morphologies of LiFePO_4 : relevance to electrochemical behaviour. *Journal of Materials Chemistry*, 18(11), 1209-1215.
- [24] Yang, J., & Tse, J. S. (2011). Li ion diffusion mechanisms in LiFePO_4 : an ab initio molecular dynamics study. *The Journal of Physical Chemistry A*, 115(45), 13045-13049.
- [25] Zhang, P., Wu, Y., Zhang, D., Xu, Q., Liu, J., Ren, X., Luo, Z., Wang, M. & Hong, W., (2008). Molecular dynamics study on ion diffusion in LiFePO_4 olivine materials. *The Journal of Physical Chemistry A*, 112(24), 5406-5410.
- [26] Huttin, M., & Kamlah, M. (2012). Phase-field modeling of stress generation in electrode particles of lithium ion batteries. *Applied Physics Letters*, 101(13), 133902.
- [27] Warren, J. A., Kobayashi, R., Lobkovsky, A. E., & Carter, W. C. (2003). Extending phase field models of solidification to polycrystalline materials. *Acta Materialia*, 51(20), 6035-6058.
- [28] Voter, A. F., Montalenti, F., & Germann, T. C. (2002). Extending the time scale in atomistic simulation of materials. *Annual Review of Materials Research*, 32(1), 321-346.
- [29] Montalenti, F., & Voter, A. F. (2001). Applying accelerated molecular dynamics to crystal growth. *physica status solidi (b)*, 226(1), 21-27.
- [30] Balakrishna, A. R., & Carter, W. C. (2018). Combining phase-field crystal methods with a Cahn-Hilliard model for binary alloys. *Physical Review E*, 97(4), 043304.
- [31] Elder, K. R., & Grant, M. (2004). Modeling elastic and plastic deformations in nonequilibrium processing using phase field crystals. *Physical Review E*, 70(5), 051605.
- [32] Zhu, C., Gu, L., Suo, L., Popovic, J., Li, H., Ikuhara, Y., & Maier, J. (2014). Size-Dependent Staging and Phase Transition in $\text{LiFePO}_4/\text{FePO}_4$. *Advanced Functional Materials*, 24(3), 312-318.
- [33] Nakamura, A., Furutsuki, S., Nishimura, S.I., Tohei, T., Sato, Y., Shibata, N., Yamada, A. and Ikuhara, Y. (2014). Phase Boundary Structure of Li_xFePO_4 Cathode Material Revealed by Atomic-Resolution Scanning Transmission Electron Microscopy. *Chemistry of Materials*, 26(21), 6178-6184.
- [34] Hillert, M., & Staffansson, L. I. (1970). Regular-solution model for stoichiometric phases and ionic melts. *Acta Chem. Scand.*, 24(10), 3618-3626.
- [35] Emmerich, H., Löwen, H., Wittkowski, R., Gruhn, T., Tóth, G. I., Tegze, G., & Gránásy, L. (2012). Phase-field-crystal models for condensed matter dynamics on atomic length and diffusive time scales: an overview. *Advances in Physics*, 61(6), 665-743.
- [36] Ofori-Opoku, N., Fallah, V., Greenwood, M., Esmaeili, S., & Provatas, N. (2013). Multicomponent phase-field crystal model for structural transformations in metal alloys. *Physical Review B*, 87(13), 134105.
- [37] Cahn, J. W. (1977). Critical point wetting. *The Journal of Chemical Physics*, 66(8), 3667-3672.
- [38] Tang, M., Carter, W. C., Belak, J. F., & Chiang, Y. M. (2010). Modeling the competing phase transition pathways in nanoscale olivine electrodes. *Electrochimica Acta*, 56(2), 969-976.
- [39] Padhi, A. K., Nanjundaswamy, K. S., & Goodenough, J. B. (1997). Phospho-olivines as positive-electrode materials for rechargeable lithium batteries. *Journal of the electrochemical society*, 144(4), 1188-1194.
- [40] Martin, J. W., Doherty, R. D., & Cantor, B. (1997). *Stability of microstructure in metallic systems*. Cambridge University Press.
- [41] Winning, M., Gottstein, G., & Shvindlerman, L. S. (2002). On the mechanisms of grain boundary migration. *Acta Materialia* 50(2), 353-363.
- [42] Janssens, K. G. F., Raabe, D., Kozeschnik, E., Miodownik, M. A., & Nestler, B. (2010). *Computational materials engineering: an introduction to microstructure evolution*. Academic Press.
- [43] Gottstein, G., King, A. H., & Shvindlerman, L. S. (2000). The effect of triple-junction drag on grain growth. *Acta materialia*, 48(2), 397-403.
- [44] Gottstein, G., & Shvindlerman, L. S. (2009). *Grain boundary migration in metals: thermodynamics, kinetics, applications*. CRC press.
- [45] Balke, N., Jesse, S., Morozovska, A. N., Eliseev, E., Chung, D. W., Kim, Y., Adamczyk, L., Garcia, R. E., Dudney, N., & Kalinin, S. V. (2010). Nanoscale mapping of ion diffusion in a lithium-ion battery cathode. *Nature Nanotechnology*, 5(10), 749-754.
- [46] Ulvestad, A., Singer, A., Clark, J.N., Cho, H.M., Kim, J.W., Harder, R., Maser, J., Meng, Y.S. and Shpyrko, O.G. (2015). Topological defect dynamics in operando battery nanoparticles. *Science*, 348(6241), pp.1344-1347.
- [47] Narayan, T. C., Hayee, F., Baldi, A., Koh, A. L., Sinclair, R., & Dionne, J. A. (2017). Direct visualization of hydrogen absorption dynamics in individual palladium nanoparticles. *Nature communications*, 8, 14020.
- [48] Perumal, R., Kubendran Amos, P. G., Selzer, M., & Nestler, B. (2018). Phase-field study of the transient phenomena induced by ‘abnormally’ large grains during 2-dimensional isotropic grain growth. *Computational Materials Science*, 147, pp. 227-237.
- [49] Aland, S., Hatzikirou, H., Lowengrub, J., & Voigt, A. (2015). A mechanistic collective cell model for epithelial colony growth and contact inhibition. *Biophysical journal*, 109(7), 1347-1357.
- [50] Morgan, D., Van der Ven, A., & Ceder, G. (2004). Li conductivity in Li_xMPO_4 (M= Mn, Fe, Co, Ni) olivine materials. *Electrochemical and solid-state letters*, 7(2), A30-A32.
- [51] Provatas, N., Dantzig, J. A., Athreya, B., Chan, P., Stefanovic, P., Goldenfeld, N., & Elder, K. R. (2007). Using the phase-field crystal method in the multi-scale modeling of microstructure evolution. *Jom*, 59(7), 83-90.
- [52] Kundin, J., & Choudhary, M. A. (2017). Application of the anisotropic phase-field crystal model to investigate the lattice systems of different anisotropic parameters and orientations. *Modelling and Simulation in Materials Science and Engineering*, 25(5), 055004.
- [53] Prieler, R., Hubert, J., Li, D., Verleye, B., Haberkern, R., & Emmerich, H. (2009). An anisotropic phase-field crystal model for heterogeneous nucleation of ellipsoidal colloids. *Journal of Physics: Condensed Matter*, 21(46), 464110.